High-speed Videomicroscopy of Sheared Carbonyl Iron Suspensions

Óscar Martínez-Cano[1], Jose R. Morillas[1], Martin Cvek[2],

Javier Ramírez[3] and Juan de Vicente[1]*

[1] F2N2Lab, Magnetic Soft Matter Group and Excellence Research Unit 'Modeling Nature' (MNat), Department of Applied Physics, Faculty of Sciences, University of Granada, C/Fuentenueva s/n, 18071 - Granada, Spain

[2] Centre of Polymer Systems, University Institute, Tomas Bata University in Zlín, tř. Tomáše Bati 5678, 760 01 - Zlín, Czech Republic

[3] Department of Signal Theory Networking and Communications, School of Technology and Telecommunications Engineering, University of Granada, C/ Periodista Daniel Saucedo Aranda s/n, 18014 - Granada, Spain

*jvicente@ugr.es

Keywords:

Magnetorheology, Magnetorheological fluids, Flow-field superposition, Start-up, Layered pattern, Mason number, stripes.

Abstract

The postyield rheological regime is investigated in sheared magnetic field-responsive composites (i.e. carbonyl iron based magnetorheological fluids). When subjected to uniaxial DC fields, high-speed videomicroscopy techniques and dedicated image analysis tools demonstrate that dispersed magnetic microparticles self-assemble to form concentric layered patterns above a particular shear rate ($\dot{\gamma}_{R,c}$). This critical shear rate for layer formation is dictated by a critical Mason number $Mn_c \sim 1$ that is associated to the destruction of the last doublet in the chain-like aggregates. The number of layers, mean width, percentage of occupation and mean period are found to be very weakly dependent on the shear rate in start-up shearing flow tests. Experimental data for the mean period are in good agreement with an energy minimization theory.

1. Introduction

Conventional magnetorheological (MR) fluids are smart composites consisting of magnetizable microparticles dispersed in a non-magnetic Newtonian liquid carrier. In the absence of magnetic fields, the suspensions behave as regular non-Brownian suspensions. However, in the presence of magnetic fields, particles become magnetized and aggregate to form chain-like structures in the field direction [1,2]. Interestingly, other patterns, apart from those elongated structures, can be obtained by a combination of flow and field configurations. For instance, layered patterns have been reported in three different scenarios [3]: i) constant magnetic field and oscillatory shear flow, ii) rotating magnetic field and no flow and iii) constant magnetic field and steady shear

flow. In this manuscript, we are interested in expanding the current knowledge concerning the third possibility by carefully studying the formed structures through dedicated image analysis techniques.

In the absence of a flow kinematics, particles aggregate into oriented chain-like structures under uniaxial DC fields. However, in the presence of steady shearing flows, these field-induced structures break (at the yield point), and the viscosity decreases. This shear-thinning behavior in the postyield regime is dictated by only two dimensionless numbers: the particle volume fraction ϕ and the Mason number Mn [4,5]. Unfortunately, the direct microscopic observation of the field-induced structures under a shear flow is hard to be performed and, as a result, very few papers have been published so far. Actually, previous work has been restricted to two particularly simple cases: small Mn and oscillatory shear [6,7] and large Mn and steady simple shear [8-10].

In the case of small Mn (lower than approx. 0.3), Cutillas and coworkers [6,7] reported the formation of a periodic layered pattern in the flow direction under oscillatory shear for strains above a critical value $\gamma_c \sim 0.15$. Stripes separate (and do not coalesce) due to repulsive forces between surface magnetic charges in each individual stripe. γ_c was found to be independent of the cell thickness, the field strength and the Peclet number. Moreover, the mean period of the layers was predicted from energy minimization even though the structure was formed by the flow-field superposition. The mean period of the pattern decreased with the particle concentration and increased with the field strength and the gap size.

In the case of large Mn (till approx. 15), Volkova and coworkers [8-10] reported the formation of layered patterns along the flow field in steady shear using cone-plate geometries. The appearance of these layers was associated with a critical shear rate $\dot{\gamma}_c$ (for a critical Mason number $Mn_c \sim 1$) and the breakage of the last doublet in the suspension. Unfortunately, a quantitative analysis of the observed structures was not reported in their paper. Similar layers have been observed in numerical simulation studies on electrorheological fluids, e.g. [11], and magnetorheological fluids [12-14]. In this case, the cut-off radius considered in the computation of the magnetic interactions between particles seems to affect the period and thickness of the layers.

Interestingly, in most of the previous publications, high-speed cameras are not used and patterns are not visualized directly under shear but at the end of the test once the sample is removed from the rheometer, e.g. [15]. Typically, suspensions are prepared in paraffin wax and start-up experiments run at a temperature well above the melting point of the wax. Then, the rotation is stopped, and the sample allowed to cool down for the wax to solidify. Finally, the sample is removed from the rheometer and visualized under a microscope. For the first time, in this manuscript, we carry out high-speed videomicroscopy observations in synchronization with acquisition of rheological data of carbonyl iron based MR fluids subjected to simple shear flows and large Mn under the presence of uniaxial DC fields. High-speed imaging is needed for the structures to be frozen at large Mn. Also, start-up (unsteady) tests are investigated as a first step towards the full understanding of these materials under a steady shear kinematics. The obtained time-resolved images are carefully analyzed to get quantitative morphological information of the formed layers: number, mean width, percentage of occupation and

mean period. The experimental results are discussed in terms of energy minimization arguments.

2. Materials and methods

MR fluids used in this work were prepared by dispersion of carbonyl iron microparticles in glycerol. A particle volume fraction of 10 vol% was used; field-induced structures were too weak for smaller concentrations while the suspensions were too dark for visualization at larger concentrations. The microparticles were provided by BASF SE (Germany). They were grade EW with a typical diameter of 3 μm and a density of 7.86 g/cm^3. Glycerol (86-88%, 1.232 g/cm^3, 106 mPa·s at 25 ºC) was purchased from Scharlau (Spain).

Rheological experiments were carried out in a MCR 501 stress-controlled torsional rheometer (Anton Paar, Austria), using a plate-plate configuration. The gap between the plates was fixed at 300 μm. The upper plate was made of titanium (radius $R = 10$ mm) and its surface was sandblasted to minimize wall slip. The bottom plate consisted of a transparent smooth glass. Experiments were performed at room temperature (~25 º C) and the magnetic field was generated in the velocity gradient direction using an open coil surrounding the sample.

Just before each measurement, samples were prepared and thoroughly dispersed using a vortex mixer (3000 rpm, 30 s) and an ultrasonic bath (30 s). Then, 0.1 mL of the MR fluid was injected by a micropipette on top of the glass plate, and the upper plate was

displaced downwards to confine the MR fluid at the desired gap. The measurement protocol was as follows. First, a preshear was applied at a constant shear rate of 100 s^{-1} during 60 s. Then, the preshear stopped and a magnetic field of 10.81 $kA \cdot m^{-1}$ was suddenly applied during 60 s to structure the suspension. Finally, a start-up test was initiated imposing a constant shear rate, still in the presence of the magnetic field. During the last interval, the shear stress was monitored as a function of time while images were recorded. The number of acquired data points was 120, and they were taken in logarithmically distributed time intervals from 0.1 s to 10 s to better resolve the short time response. With this, each test took 261 s in total. Experiments were repeated at least three times with fresh new samples.

Video-microscopy observations were carried out through the glass bottom plate using a high-speed camera FASTCAM Mini UX50 (Photron, Japan) with a 1.3-Megapixel CMOS sensor, coupled to an optical system composed by a Navitar 1-60123 6.5X Zoom with a 1-6218 1.0X Standard Adapter. In this work, the sample was homogeneously illuminated using a LED ring GX-860 with 61 mm diameter. The dark-field illumination provided by this ring facilitated the visualization of the particle structures by increasing the exposure of their surface in contact with the bottom glass and making them brighter than the surface of the upper plate. The shutter of the camera was set to 1/125 s. This was sufficiently fast to freeze the layers at the largest investigated shear rates and sufficiently slow to get pictures clear enough to properly detect and analyze the layers with a custom-built image analysis software. Both a dark-field illumination and a fast shutter speed were critical to get high-quality video-microscopy data in flowing MR fluids.

Image capture and rheological data acquisition were synchronized using two analog outputs of the rheometer, one for the trigger of the camera to indicate when the experiment started and the other for the synchronization signal that indicated to the camera when to take pictures. Figure 1 shows the schematics of the setup used in this work.

3. Image analysis

Figure 2 shows a typical raw image with a dimension of 1280 × 1024 pixels corresponding to the layered pattern observed in an MR fluid subjected to superimposed shear and magnetic fields. Due to the dark-field illumination, dark regions in Figure 2 correspond to particle depleted areas while light regions correspond to particle rich areas. As observed, the iron microparticles arrange in concentric circular layers, around the geometric center, oriented in the flow field direction. The employed setup and magnification are such that a single frame provides information about the layer formation along the complete radius of the plate (approximately 1.5×). Before each experiment, a precision calibration target was placed in the sample position to calibrate the pixel size. A homemade Matlab script was written to perform the calibration and to automatically analyze all the images obtained in the experiments.

Next, the image processing method is explained using the image shown in Figure 2. As a first step, the obtained RGB images are converted to grayscale images. The picture that is shown in Figure 2 already looks like a grayscale image, but it is truly an RGB file so that not too much information is lost in its conversion to an intensity image. Note that

an RGB file is treated as an M × N × 3 matrix while a grayscale image has a dimension M × N with intensity values from 0 to 255. After grayscale conversion, the script computes the complement of the images with the aim of matching the color of the particle layers in the image to the real blackish color of the particles. In this process each pixel value is subtracted from the maximum pixel value supported by the class, and the difference is used as the pixel value in the output image. In the output image, dark areas become lighter and light areas become darker. After this process, the dark regions will now correspond to areas rich in particles.

The next step consists in sharpening the layers in the picture to facilitate their detection using the unsharp masking method [16]. Generally speaking, in this technique a fraction of the blurred version of the image is added to itself to form the improved version. It improves the spatial resolution by sharpening object boundaries at the cost of image noise. In practice, this filter depends on two parameters: the standard deviation of Gaussian lowpass filter and the strength of sharpening effect. The employed values for them (15 for both) were chosen among 400 combinations looking for those values providing the best output when the filter is applied to a converted grayscale image. Figure 3a shows the result of applying the unsharp masking method to Figure 2. Because of the high values of the parameters chosen for the filter, Figure 3a already looks like a black and white image, which is required to compute the metrics during the layer formation process, but it is still a grayscale image. To convert it to a pure black and white image the Otsu's method is used [17]. This method computes a global threshold by maximizing the between-class variance of the segmented classes. This threshold is used to convert the intensity image to a binary image. Figure 3b shows the final black and white image after applying Otsu's method to Figure 3a.

Metrics of interest in this work are the number of layers, their mean width, the percentage of occupation along the radius of the geometry and the mean period of the pattern. In their computation, we take advantage of the cylindrical symmetry in the pictures. Images are transformed to polar coordinates fixing the origin at the geometric center of the pattern and associating a new coordinate (ρ, θ) to each pixel (x, y) of the image. The new coordinates must also be placed into a square matrix to work with them. Thus, the script interpolates a surface with a dimension equal to the range of ρ and θ at the query points specified by the polar coordinates using a triangulation-based natural neighbor method. From a computational point of view this is the most expensive step in the image analysis process. The transformation from Cartesian to polar images is shown in Figure 4. As observed, the circular layers become a vertical stripe pattern. However, some defects appear in the image as well. Firstly, there is a black region that corresponds to an area without information. Secondly, there is a gray region generated by the extrapolation of the pixel at the edge of the Cartesian picture. Finally, in the layered pattern some lobes appear whose shape only depends on the place (with respect to the Cartesian image center) where the origin of the coordinate reference system is defined.

The objective now is to average the image intensity in the θ component collapsing the picture in a single (radial) section that informs about the layer distribution and morphology along the geometry radius. Previously, it is necessary to find a mechanism in order not to consider the defects of the polar image. The solution for this problem is to create a mask from the polar image to avoid the spurious areas. As we can see in Figure 4, the white layers (corresponding to particle depleted areas) are a unique

characteristic in this picture. Hence, applying a closing morphological operation with a 250-pixel square structural element (which is suitable for the typical width of the layers found in our images), a dilatation effect of the white pixel in the horizontal direction is achieved. Later, we can delete all the pixels that are not white, generating the mask needed to get rid of the mentioned defects. Figure 5 shows the mask obtained for our sample image. It is important to comment that it is not necessary to generate a mask for each image because the shape of the spurious area generated in the interpolation process does not change during an experiment. As a result, the same mask can be used for all pictures of a given experiment.

Now, it is possible to calculate the average in θ, but only considering the part of the polar image with layer information, by overlapping the polar image with its mask. This process generates the masked polar image that is shown in Figure 6a. Here the disregarded area for the average of the θ component has been painted gray color. In Figure 6b it is shown the radial section result of the average of the layered area represented as a row grayscale image. Ideally, if the layers in Figure 6a were perfectly vertical, the results of the average would be binary (black or white depending on there is or not a layer). Nevertheless, there are pixel columns of the masked polar image that have both black and white pixels. This is so because the layers in the original image are not perfectly round nor/or concentric. So, after the averaging process, it is necessary to do another binary conversion of the mean radial section. In this case, the threshold used for the binarization is half of the range of the class (125). The resultant radial section image is shown in Figure 6c and its pixel value profile can be seen in Figure 7a. Note that the second binarization is useful to clearly delineate the layer edges but it can also introduce some artifacts. For example, if the radial section does not contain the layer

pattern but a homogeneous intensity profile, any small variation above/below the threshold value of 125 will be directly translated to a white/black pixel and hence understood as the absence/presence of a layer (even though the original profile does not contain any of them).

Once the binary radial section is generated (see Figure 6c) the aforementioned metrics can be calculated from it. The first one is the number of layers, computed by identifying as a layer each group of contiguous black pixels (regardless the group width). The second metric is the mean width of the layers. This corresponds to the average number of pixels of all identified groups. The third metric is the percentage of occupation. It represents the ratio between the number of black pixels and the total number of pixels in the binary mean radial section. This metric can be calculated also from the black and white Cartesian image (i.e. before polar coordinates transformation, masking, θ-average and second binarization) and, hence, it can be used as a reference to verify whether the image treatment from Figure 3b to Figure 6c introduces severe artifacts or not. As it can be seen in Figure S1 of the Supplementary Material, the percentage of occupation computed from both kinds of images shows no significant differences indicating that the employed image processing method is not distorting the information contained in the original pictures. The fourth and last metric is the mean period of the layered pattern. This is computed using the Fast Fourier Transform [18]. The black line in Figure 7b corresponds to the modulus of the FFT obtained for the binary average of our sample image (Figure 7a). The red line in Figure 7b is the result of applying a third-order one-dimensional median filter to the FFT module. The maximum of this signal is selected as the average harmonic which provides the mean spatial frequency and therefore the mean period of the layered pattern. At this point it is worth to note that the

FFT computation was double-checked computing the autocorrelation of the binary mean radial section (see Figure S2). Both methods yield similar results.

In practice, as stated above, we are interested in exploring microstructural changes with time under a prescribed flow kinematics (i.e. a start-up test). This requires capturing many pictures, like that shown in Figure 2, and processing them. In this sense, the software can also construct summary images by concatenating the mean radial sections (Figure 6c) of the consecutive pictures taken during a test. An example can be found in Figure 8. The upper panel of Figure 8 describes the start-up kinematics (a constant rim shear rate of $\dot{\gamma}_R = 400$ s^{-1}). The second panel shows the shear stress generated by the MR fluid at the rim of the plate (τ_R). Finally, the bottom panel of Figure 8 shows the summary image obtained by concatenation of radial sections. Note that the mean radial sections have been cropped previously at 9.8 mm to avoid the noticeable compression and dilatation effect of the sample in the radial direction, produced in the rim of the geometry by its eccentricity. Also, the width of each mean radial section has been properly adapted to fit the logarithmic distribution of the data points taken by the rheometer.

4. Theoretical model

In order to theoretically predict the period of the pattern, d, an energy minimization model proposed by Cutillas *et al*. [6,7] is used. This model assumes that the particles (radius a) are arranged into layers with a given internal volume fraction, ϕ_a, that expand the whole shearing gap h. The model assumes that hydrodynamic forces play a secondary role allowing the particles to reach minimum energy states but not breaking

the structures formed under the magnetic field. Thus, by simply minimizing the magnetostatic energy of the pattern it is possible to find the equilibrium pattern period. Two ingredients are considered for the magnetic energy computation: volumetric and surface contributions [7,19].

Volumetric energy simply comes from the magnetization $\vec{M}$ acquired by the layers when the pattern is exposed to an external magnetic field $\vec{H}$. Supposing that magnetic particles are linear, with relative permeability μ_{pr}, and that each layer is homogenously magnetized, the volumetric energy per unit volume is given by:

$$u_V = -\frac{1}{2}\varphi\vec{M}\bullet\vec{H} = -\frac{1}{2}\mu_0\varphi H^2\frac{3\beta\phi_a}{1+3\beta\phi_a(D-1/3)} \quad (1)$$

where μ_0 is the vacuum permeability, $\varphi = \phi/\phi_a$ is the apparent volume fraction of the layers, ϕ is the particle volume fraction, β is the contrast factor $\beta = (\mu_{pr} - \mu_{cr})/(\mu_{pr} + 2\mu_{cr})$, μ_{cr} is the carrier relative permeability and D is the pattern demagnetization factor. The latter only depends on the layer geometrical parameters, φ and $d^* = d/h$, and accounts for the perturbation on the external field due to the layer magnetization. The demagnetization factor reads as follows:

$$D\left(\varphi, d^*\right) = \varphi + \frac{d^*}{\pi^3\varphi}\sum_{n=1}^{\infty}\frac{(n\pi\varphi)}{n^3}\left[1 - \exp exp\,(-2\pi n/d^*)\right] \quad (2)$$

Surface energy effects appear due to the weaker local field experienced by the particles at the layer surface in comparison to particles within the bulk of the layer. Based on a

mean-field computation, the difference between those fields is $H_V - H_s = \frac{M}{6\mu_0}$. If it is supposed that only particles at the external surface of the layer are exposed to H_s, the surface energy per unit volume can be written in terms of the layer bulk magnetization M as:

$$u_S = \frac{2}{3}\frac{M^2}{\mu_0}\frac{a}{d} \tag{3}$$

Supposing that the apparent volume fraction of the layers does not depend on the period and imposing the condition for minima to the total magnetic energy $\frac{\partial(u_V+u_S)}{\partial d}\Big|_{\varphi} = 0$, the following equation for the pattern period is obtained:

$$\varphi\frac{\partial D}{\partial d^*} = \frac{4a}{3h\left(d^*\right)^2} \tag{4}$$

5. Rheomicroscopy

Rheological experiments described in this manuscript consist in start-up tests in the classical plate-plate configuration. Under this particular kinematics, a constant rim shear rate is applied and the resulting stress is measured as a function of time. An example is shown in Figure 8 for a rim shear rate of $\dot{\gamma}_R = 400$ s^{-1}.

As observed in Figure 8, the stress initially shows a high scattering in the data and then, at a given time (t~10 s), levels off at a constant steady value. This behavior is in very

good qualitative agreement with experiments on electrorheological fluids by Vieira *et al.* [20]. The stabilization of the stress is clearly concurrent with the formation of a steady pattern along the plate radius. The sole exception is the appearance of unstable layers in the proximity of the rim ($\rho \sim 8.5 - 9.8$ mm) due to the slight and unavoidable eccentricity and misalignment of the geometries there. As shown in the bottom panel of Figure 8, the layers form essentially at the same time (t~10 s) over the whole surface.

A priori, there are three plausible explanations for the high scattering in the transitory regime: short data acquisition time (i.e. logarithmic duration time from 0.1 s to 10 s), sample specificities (i.e. layer formation/destruction) and a combination of both. To clarify the reason for such a large scattering we also carried out start-up tests with a silicone oil (not containing particles) exhibiting a comparable stress response as the MR fluid under similar conditions to those reported in Figure 8. The stress curve for the oil (Figure S3) was also noisy up to 10 s but the standard deviation of this interval is a little bit lower than the MR fluid: 5.6 Pa for the oil vs. 8.5 Pa for the MR fluid. As a result, the large scattering at short times seems to be mainly due to the short acquisition time of the rheometer at the beginning of the experiment, but the sample specificities are also involved.

As shown in Figure 8, a random sequence of tiny black stripes appears in the transitory regime. These stripes are indeed noise. At these initial stages, the microstructure actually consists of chain-like aggregates in the field direction that are homogeneously distributed over the sample (the shear flow does not have time to reorganize them). Hence, the radial section obtained from the polar component average is homogeneous as

well (with an intensity value close to 125) and it does not show any pattern. As mentioned previously, the binarization of this kind of radial sections has an associated error that produces 'false' layer identification and, consequently, the observable random sequence of tiny stripes. Of course, when computing the metrics, these radial sections obtained during the transitory regime are not considered.

Figure S4a shows stress versus time curves in start-up tests for a range of rim shear rates in the interval $\dot{\gamma}_R \in [100, 500]$ s^{-1}. The associated stress vs. time curves are qualitatively similar to Figure 8 no matter the applied shear rate value. Figure S4b shows the corresponding summary images. Interestingly, for the explored shearing time (261 s), stable layers do not form if $\dot{\gamma}_R < 300$ s^{-1}. Contrarily, for $\dot{\gamma}_R \geq 300$ s^{-1} well-defined stable layers appear. Again, a clear correlation is found between the stress stabilization and the appearance of the layers.

Additional experiments were carried out to interrogate the influence of shearing time at the lowest investigated shear rates where stable layers did not form. Figure S5 compares the results for three different rim shear rates (100 s^{-1}, 200 s^{-1} and 400 s^{-1}) in experiments with a duration time of 1290 s. The summary pictures shown in Figure S5 demonstrate that formed layers at lowest shear rate are not a stable but appear and disappear during the test. These experiments suggest that the formation of the layers does not depend only on the shearing time, but it also depends on the relative importance of the hydrodynamic forces over magnetostatic ones.

The ratio between the hydrodynamic drag force and the magnetic interparticle force triggered by the magnetic field is commonly known as the Mason number, Mn. In the

linear magnetostatic regime and using the Stokes drag approximation, it can be written as $Mn = 8\eta\dot{\gamma}/(\mu_0\mu_{cr}\beta^2H^2)$, where η is the carrier fluid viscosity and $\dot{\gamma}$ the imposed shear rate. With this in mind, layers are expected to appear only when Mn is above a critical value, $Mn_c \sim 1$. This corresponds to a critical shear rate capable to disrupt a doublet of particles formed by the magnetic field [8]. Under the dipolar approximation the critical Mason number is $Mn_c = 0.938$ and hence the critical shear rate would be $\dot{\gamma}_c = 66.2$ s^{-1}. This is clearly a far too low shear rate for layer formation in view of the experimental results shown in Figure S4 that suggest a critical shear rate of approximately 300 s^{-1}.

A more precise estimation of the critical shear rate requires the inclusion of multipolar contributions in the magnetostatic interactions [21]. In this case, the critical Mason number reads as follows [8]:

$$Mn_c = \frac{1.581\sqrt{f_{||}f_{\Gamma}}}{\sqrt{2.038+0.8f_{\perp}/f_{\Gamma}}} \quad (5)$$

Here $f_{||}$, $f_{\perp}$ and f_{Γ} are dimensionless functions accounting for the effects of multipoles over the dipolar interaction. These functions depend on the interparticle distance and the contrast factor β. For an interparticle distance equal to the particle diameter and the external magnetic field employed in this work, $H = 10.81$ kA/m, one obtains $\beta = 0.64$ and hence, $f_{||} = 4.56$, $f_{\perp} = 0.70$ and $f_{\Gamma} = 1.31$ (values interpolated from [22]). With this, the critical Mason number provided by equation 5 becomes $Mn_c = 2.47$ and the

corresponding critical shear rate $\dot{\gamma}_c = 175$ s^{-1}. The latter is still smaller than the experimental one.

In order to compare with the experiments, it should be borne in mind that the shear rate in a plate-plate configuration is not homogeneous. On the contrary, it increases linearly along the plate radius $\dot{\gamma}(\rho) = \dot{\gamma}_R \rho / R$, being R the plate radius and $\dot{\gamma}_R$ the rim shear rate. Thus, for a rim shear rate of $\dot{\gamma}_R = 200$ s^{-1}, only 25% of the sample is really sheared with a shear rate larger than the critical one. This could explain why at this shear rate the layer pattern shown in Figure S5 is not completely stable in time. To take the radial profile of the shear rate into consideration, the previous computation of the critical shear rate can be done in terms of the effective (mean) shear rate $\langle\dot{\gamma}\rangle$ experienced by the sample in the plate-plate configuration. Such approximation has been done previously in the literature to evaluate the effect of non-homogeneous magnetic field profiles [23]. In this case, since the shear rate profile is linear, its mean value is one half of the rim shear rate, $\langle\dot{\gamma}\rangle = \dot{\gamma}_R/2$. Therefore, only for rim shear rates above 2 × 175 s^{-1} ($\dot{\gamma}_R \sim$ 300 s^{-1} as seen experimentally) layers are expected. Besides, note that approximating the true shear rate in the sample by its mean value is also supported by the fact that layers appear along the radial section all at once (see Figure 8).

Experiments for 300 s^{-1}, 400 s^{-1} and 500 s^{-1} were analyzed for layer formation using the image analysis software. Figure 9 shows the number of layers (a), mean layer width (b), percentage of occupation (c) and mean period of the pattern (d) during the start-up tests. Generally speaking, all those metrics consistently share the same features, they do not depend strongly on the shear rate, are constant throughout the experiment (thus, layers

do not merge/split or coarsen) and are sensitive to the pattern reconfiguration (notice, especially the case of 300 s^{-1} at approximately 100 s, the larger error bars of Figure 9 and the pattern instability-stress drop of Figure S4). The available literature for these metrics is scarce and even contradictory. On the one hand, Volkova *et al.* [10] mention that the pattern period does not depend on the shear rate. On the other hand, experiments on ER fluids by Vieira *et al.* [24] point that the number and thickness of the layers increase with the shear rate (hence, the period should decrease). Those differences could be due to the different nature of ER fluids (where demagnetization fields are absent) and experimental time scales (experiments in this work take around 5 min while in Vieira *et al.* [24] they took at least 1 h) what could give rise to other artifacts like electrophoresis, evaporation or sedimentation.

Finally, supposing that the percentage of occupation area shown in Figure 9c is constant through the sheared sample (what can be a rough approximation), one can identify it with the apparent volume fraction of the layers, thus, $\varphi = 0.4$. Using this value together with the experimental shearing gap $h = 300$ μm and the particle radius $a = 1.5$ μm, equation 4 can be solved numerically to obtain a predicted period of $d = 140$ μm. As it can be seen, this is comparable to the experimental one shown in Figure 9d. Such a good agreement is definitely surprising, and may be fortuitous, taking into consideration the assumed approximations and more investigation is needed in this sense. In particular, future work should be focused in the influence of gap size in the generated structures.

In good agreement with the model prediction, the magnetic field strength did not influence the metrics of the layered pattern with differences of the order of the

experimental uncertainty. In Table 1 we show the results for a shear rate of 300 s^{-1} at a range of magnetic field strengths (from 5.35 to 10.81 $kA \cdot m^{-1}$). As expected, no matter the magnetic field strength, the metrics are very similar because $Mn > Mn_c$.

In order to evaluate the on-off response of the material and the layered pattern evolution we designed the following experiment. The sample was placed in the rheometer and the gap closed. No preshear was applied. The shear rate was immediately fixed at 400 s^{-1} and held for a total time of 600 s. During the shearing process, a magnetic field was superimposed for 1 minute and removed for another 1 minute. The earlier sequence was repeated for a number of predetermined magnetic field values (5.35, 8.08, 10.81, 13.53 and 16.26) $kA \cdot m^{-1}$. The shear stress was measured continuously during the procedure similarly to Ulicny *et al.* [25]. Results are shown in Figure 10.

Only for sufficiently small magnetic field strengths ($Mn > Mn_c$) a stable layered pattern formed while for larger field strengths the layers were visible but not stable. Layers disappeared in the off periods (i.e. in the absence of magnetic field). No matter the magnetic field strength, the stress rapidly changed during the off-on and on-off transitions exhibiting a very short relaxation time.

These observations are in good agreement with Volkova *et al.* [8] but in clear contradiction with experiments by Kittipoomwong *et al.* [26]. In the latter case, the torque increased rapidly (slowly) to a steady-state value for $Mn > Mn_c$ ($Mn < Mn_c$). Layers observed by Kittipoomwong only became apparent during the stress transient when $Mn < Mn_c$.

6. Conclusions

Sheared MR fluids under uniaxial DC magnetic fields exhibit the formation of concentric cylindrical layers for shear rates above a critical one. A good correlation is found between stress stabilization and layer formation as demonstrated by the summary image generated by our image analysis software. The critical shear rate is found to be dictated by the magnetostatic interactions between the particles and hydrodynamic drag through the Mason number. The geometrical properties of the pattern (number of layers, mean width, percentage of occupation and mean period of the structures) do not depend on the shear rate. A reasonably good agreement is found between the experimental mean period and the theoretical model by Cutillas *et al.* [7].

Future work may focus both in fundamental and applied research. From a fundamental point of view it is still under debate whether chain or layered models are applicable in sheared MR fluids. As a result, a mechanistic explanation behind their shear thinning behavior is still not clear. This manuscript clearly shows that particles are not randomly distributed in the suspension but instead rearrange to form layers for sufficiently large Mason numbers.

From a more practical point of view, the current manuscript sheds light on the kinematic conditions required for the layers to form. Efforts may be directed in tailoring layer formation to develop more advanced MR fluids of interest in rapidly evolving applications such as the patterning of cells in anisotropic 2D magnetic scaffolds for tissue engineering.

Acknowledgements

We acknowledge Álvaro González Rodríguez for preliminary tests on this project. This work was supported by ERDF, FEDER, MICINN AE EQC2019-005529-P and PID2019-104883GB-I00 projects, Junta de Andalucía P18-FR-2465 and A-FQM-396-UGR20 projects and (EFST)-H2020-MSCA-IF-2020 (Grant 101030666) fellowship. M.C. acknowledges the project DKRVO (RP/CPS/2022/007) funded by the MEYS of the Czech Republic.

References

[1] Morillas J R and de Vicente J 2020 Magnetorheology: a review *Soft Matter* **16(42)** 9614–9642.

[2] Terkel M and de Vicente J 2021 Magnetorheology of exotic magnetic mesostructures generated under triaxial unsteady magnetic fields *Smart Mater. Struct.* **30(1)** 014005.

[3] Volkova O, Cutillas S, Carletto P, Bossis G, Cebers A and Meunier A 1999 Flow-induced structures in magnetorheological suspensions *J. Magn. Magn. Mater.* **201** 66-69.

[4] Ruiz-López J A, Hidalgo-Alvarez R and de Vicente J 2017 Towards a universal master curve in magnetorheology *Smart Mater. Struct.* **26(5)** 4001.

[5] Morillas J R and de Vicente J 2019 DEM and FEM simulations in magnetorheology: aggregation kinetics and yield stress in magnetorheological materials and their applications *IET The Institution of Engineering and Technology* **58** 19-38.

[6] Cutillas S and Bossis G 1997 A comparison between flow-induced structures in electrorheological and magnetorheological fluids *Europhys* **40** 465-470.

[7] Cutillas S, Bossis G and Cebers A 1998 Flow-induced transition from cylindrical to layered patterns in magnetorheological suspensions *Phys. Rev. Lett.* **57** 804.

[8] Volkova O, Cutillas S and Bossis G 1999 Shear banded flows and nematic-to-isotropic transition in ER and MR fluids *Phys. Rev. Lett.* **82** 233.

[9] Volkova O, Cutillas S, Carletto P, Bossis G, Cebers A and Meunier A 1999 Flow-induced structures in magnetorheological suspensions *J. Magn. Magn. Mater.* **201(1–3)** 66–69.

[10] Volkova O, Bossis G, Carletto P and Cebers A 2001 Shear banded structures and nematic to isotropic transition in MR fluids *Int. J. Mod. Phys.* **15(6-7)** 878-885.

[11] Cao J G, Huang J P and Zhou L W 2006 Structure of electrorheological fluids under an electric field and a shear flow: experiment and computer simulation *J. Phys. Chem.* **110** 11635-11639.

[12] Wang Z, Shahrivar K and de Vicente J 2014 Creep and recovery experiments of magnetorheological fluids: experiments and simulations *J. Rheol.* **58(6)** 1725-1750.

[13] Lagger H G, Bierwisch C, Korvink J G and Moseler M 2014 Discrete element study of viscous flow in magnetorheological fluids *Rheol. Acta* **53** 417-443.

[14] Lagger H G, Breinlinger T, Korvink J G, Moseler M, Di Renzo A, Di Maio F and Bierwisch C 2015 Influence of hydrodynamic drag model on shear stress in the simulation of magnetorheological fluids *J. Non-Newtonian Fluid Mech.* **218** 16-26.

[15] Henley S and Filisko F E 1999 Flow properties of electrorheological suspensions: an alternative model for ER activity *J. Rheol.* **43** 1323-1336.

[16] Badamchizadeh M A and Aghagolzadeh A 2004 Comparative study of unsharp masking methods for image enhancement *Proceedings - Third International Conference on Image and Graphics* 27–30.

[17] Jun Z and Jinglu H 2008 Image segmentation based on 2D Otsu method with histogram analysis *CSSE* **6** 105–108.

[18] Rader C M and Maling G C 1967 What is the fast Fourier transform? *Proc. IEEE* **55(10)** 1664–1674.

[19] Promislow J H and Gast A P 1997 Low-energy suspension structure of a magnetorheological fluid *Phys.* Rev. E **56(1)** 642.

[20] Vieira S L, Pompeo Neto L B and Arruda A C F 2000 Transient behavior of an electrorheological fluid in shear flow mode *J. Rheol.* **44(5)** 1139-1149.

[21] Morillas J R and de Vicente J 2019 Yielding behavior of model magnetorheological fluids *Soft Matter* **15(16)** 3330-3342.

[22] Klingenberg D J, Van Swol F and Zukoski C F 1991 The small shear rate response of electrorheological suspensions. II. Extension beyond the point–dipole limit *J. Chem. Phys.* **94(9)** 6170-6178.

[23] Laun H M, Schmidt G, Gabriel C and Kieburg C 2008 Reliable plate–plate MRF magnetorheometry based on validated radial magnetic flux density profile simulations *Rheol. Acta* **47(9)** 1049-1059.

[24] Vieira S L, Nakano M, Henley S, Filisko F E, Pompeo Neto L B and Arruda ACF 2001 Transient behavior of the microstructure of electrorheological fluids in shear flow mode *Int. J. Mod. Phys. B* **15(6-7)** 695-703.

[25] Ulicny J C, Golden M A, Namuduri C S and Klingenberg D J 2005 Transient response of magnetorheological fluids: Shear flow between concentric cylinders *J. Rheol.* **49(1)** 87.

[26] Kittipoomwong D, Klingenberg D J, Shkel Y M, Morris J F and Ulicny J C 2008 Transient behavior of electrorheological fluids in shear flow *J. Rheol.* **52(1)** 225.

Tables

Table 1.- Characteristics of the layered structures for different magnetic fields.

H (kA·m^{-1})	Number of layers (-)	Mean width (mm)	Percentage of occupation (%)	Mean period (mm)
5.35	100 ± 4	0.030 ± 0.002	32 ± 1	0.210 ± 0.013
8.08	87 ± 13	0.043 ± 0.010	37 ± 5	0.18 ± 0.02
10.81	66 ± 6	0.059 ± 0.005	40.5 ± 1.1	0.192 ± 0.015

Figures

Figure 1.- Schematics of the experimental setup for magnetorheology and high-speed video-microscopy. The MR fluid is confined between two plates in a torsional rheometer. The magnetic field is generated using an open coil. Images are obtained through the bottom glass plate.

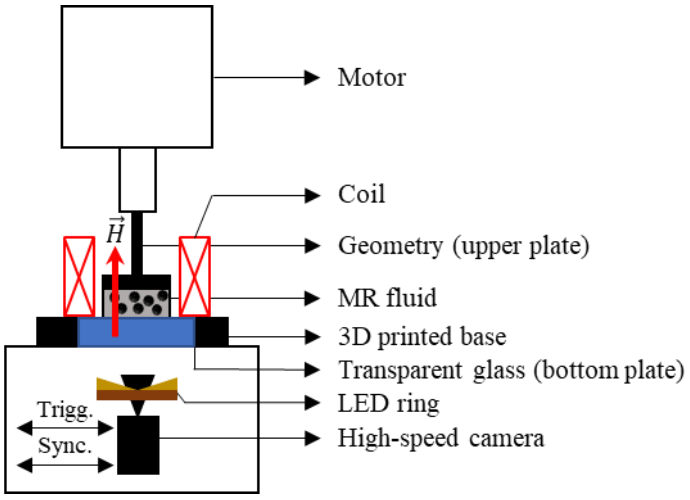

Figure 2.- Concentric layers formed in a plate-plate configuration when a magnetic field is applied in the velocity gradient direction. Particle concentration $\phi = 10$ vol%. External magnetic field strength $H = 10.81$ kA·m^{-1}. Rim shear rate $\dot{\gamma}_R = 300$ s^{-1}.

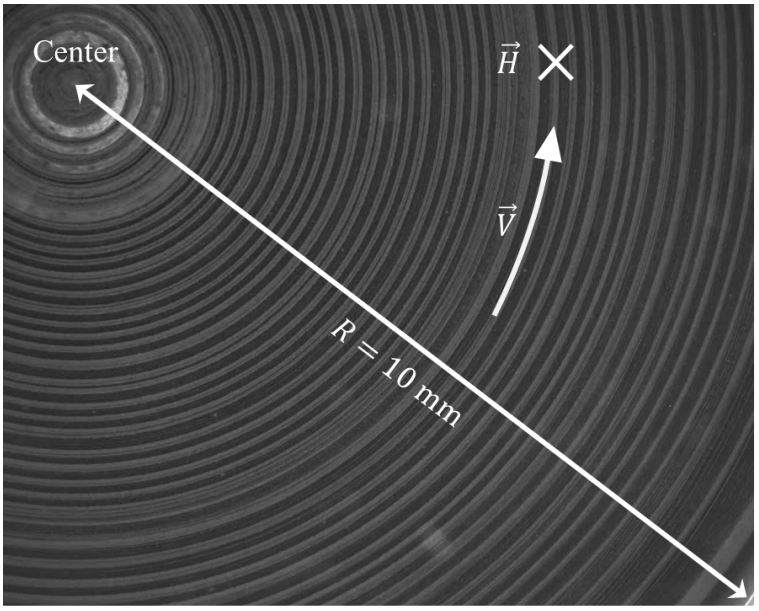

Figure 3.- (a) Result of the application of the unsharp masking method to Figure 2 to improve the spatial resolution of the original image. (b) Binary image obtained from Figure 3a after the application of Otsu's method. The bar size is 1 mm.

a) b)

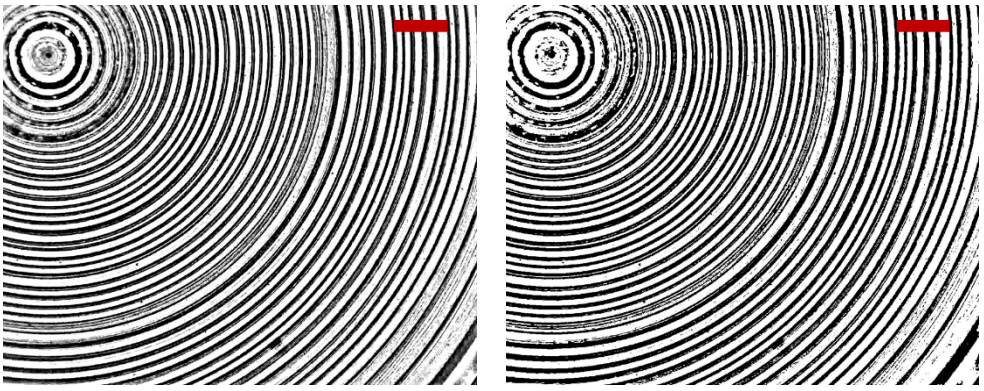

Figure 4.- Transformation of Figure 3b from Cartesian coordinates (a) to polar coordinates (b). The concentric layers transform into vertical straight layers after the process. The origin of coordinates is fixed in the center of the cylindrical pattern. The bar size is 1 mm.

a) b)

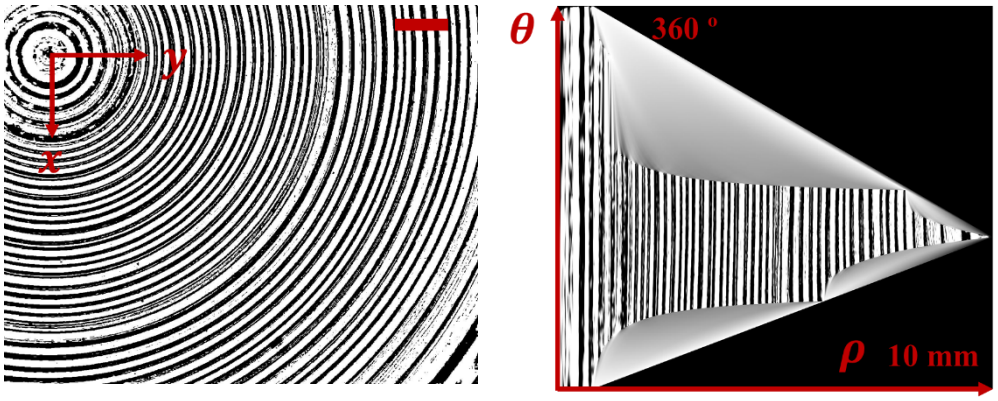

Figure 5.- Mask generated from the polar image in Figure 4b using a closing morphological operation. The bar size for the horizontal direction is 1 mm.

Figure 6.- In order not to average the defects generated by the interpolation process, the polar image is masked. (a) Masked polar image. (b) Mean radial section from θ -component average. (c) Binarization of the mean radial section. The bar size for the horizontal direction is 1 mm.

a)

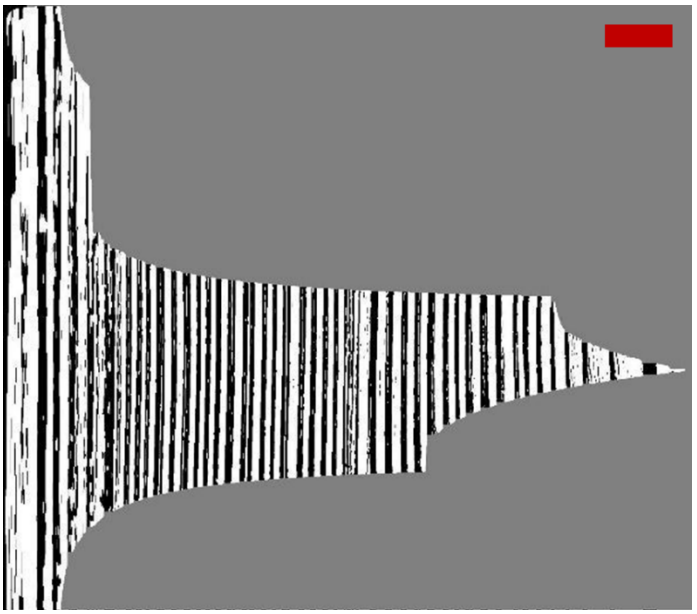

b)

c)

Figure 7.- (a) Intensity profile of the binary mean radial section of Figure 6c. (b) Fast Fourier Transform and determination of the mean period.

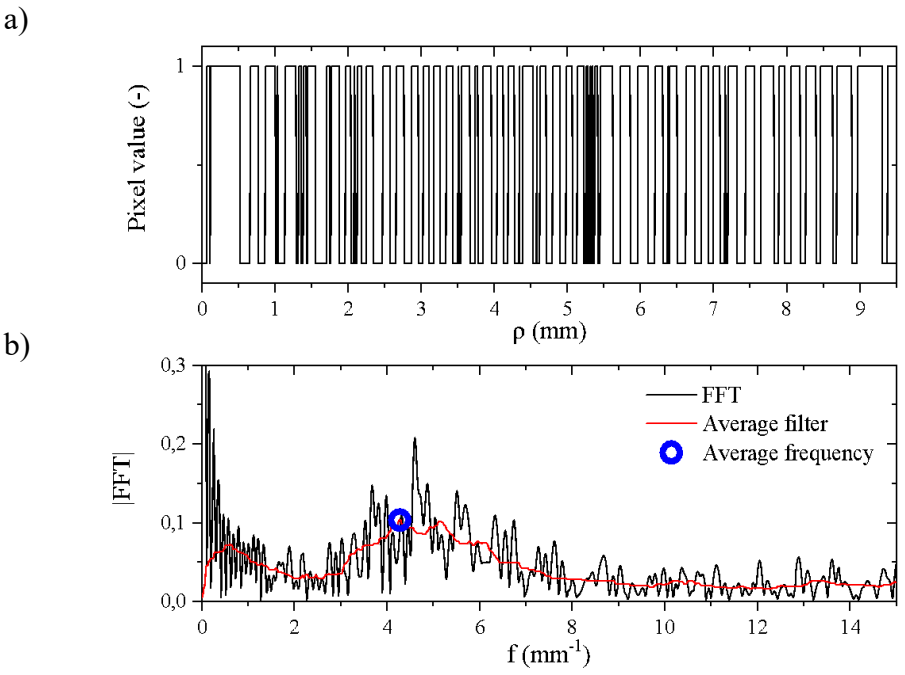

Figure 8.- Rim shear rate $\dot{\gamma}_R$, shear stress τ_R and microstructural evolution (summary image) as a function of time t during a start-up test. Particle concentration $\phi = 10$ vol%. External magnetic field strength $H = 10.81$ kA·m^{-1}. Rim shear rate $\dot{\gamma}_R = 400$ s^{-1}.

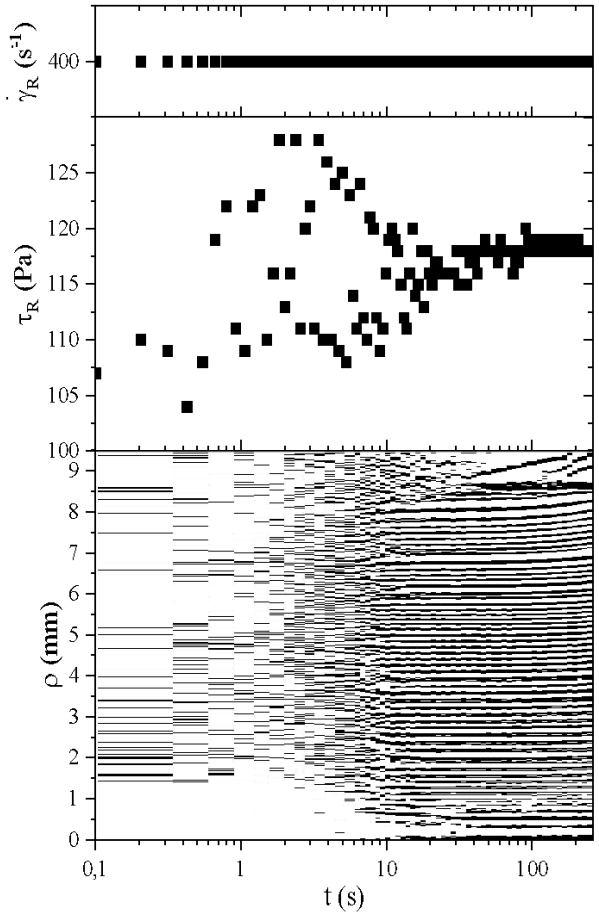

Figure 9.- Temporal evolution of the metrics during a start-up test at different rim shear rates. Error bars correspond to the standard deviation of at least three different repetitions. Particle concentration $\phi = 10$ vol%. External magnetic field strength $H = 10.81$ kA·m^{-1}. a) Number of layers, b) mean width, c) percentage of occupation and d) mean period.

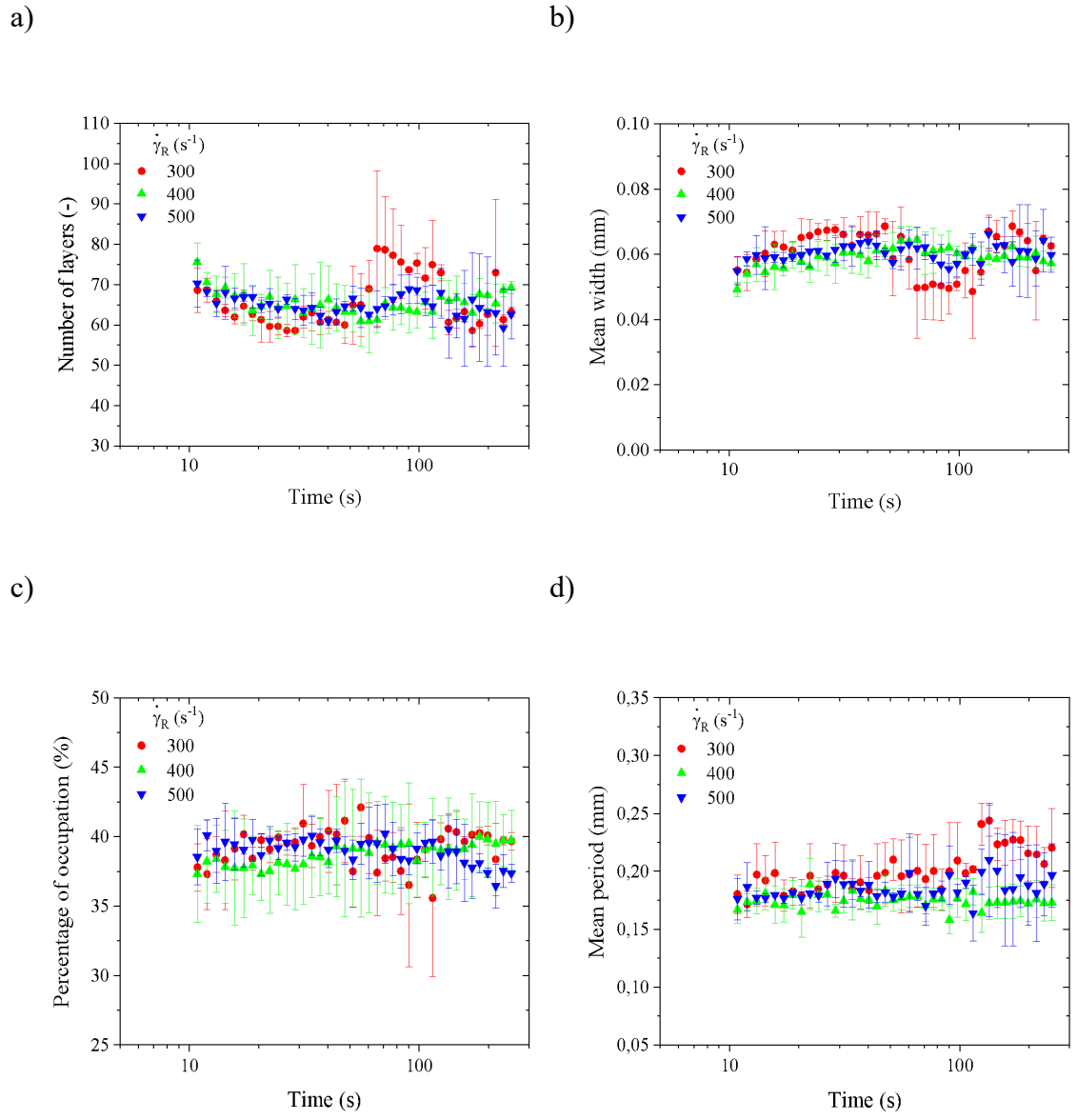

Figure 10.- Shear stress as a function of time showing the on-off and off-on behavior of the MR fluid. Photographs correspond to the stable layers observed during the on periods for $Mn > Mn_c$. Results of three different experiments on fresh new samples are shown to judge on the reproducibility in the measurements. Particle concentration $\phi = 10$ vol%. External magnetic field strength $H = 10.81$ kA·m^{-1}. Rim shear rate $\dot{\gamma}_R = 400$ s^{-1}.

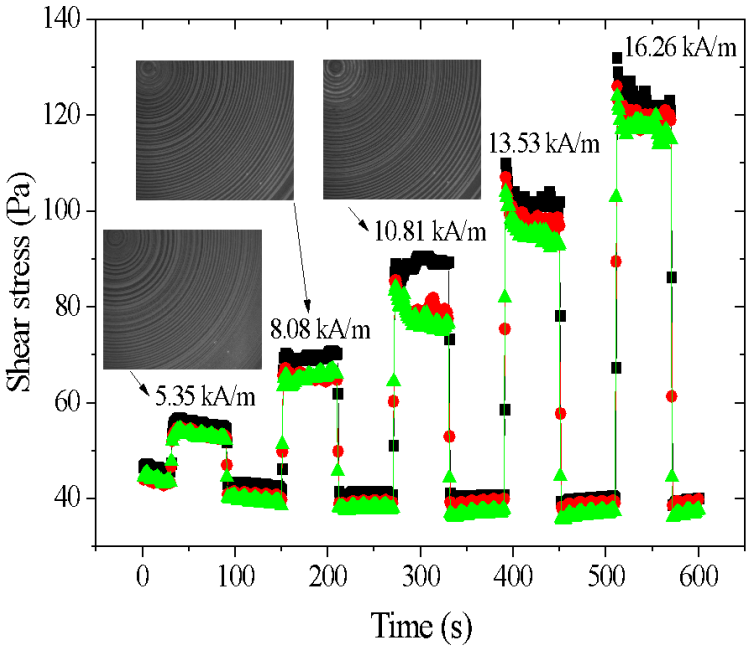

Supplementary material

Figure S1.- Double-checking the percentage of occupation (PoO) calculation: (a) Obtained from a black and white (BW) image (like Figure 3b). (b) Obtained from its mean radial section (MRS) (like Figure 6c). (c) Temporal evolution of the PoO during a start-up test using both computation approaches. Results shown in (a) and (b) correspond to the last point of the temporal evolution. Particle concentration $\phi = 10$ vol%. External magnetic field strength $H = 10.81$ kA·m^{-1}. Rim shear rate $\dot{\gamma}_R = 300$ s^{-1}.

a)

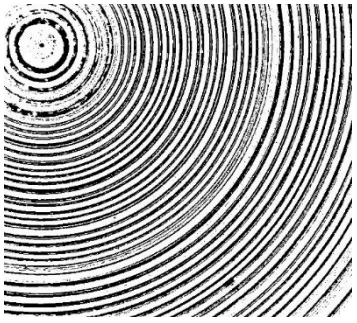

PoO (BW) = 40,95 %

b)

PoO (MRS) = 39,18 %

c)

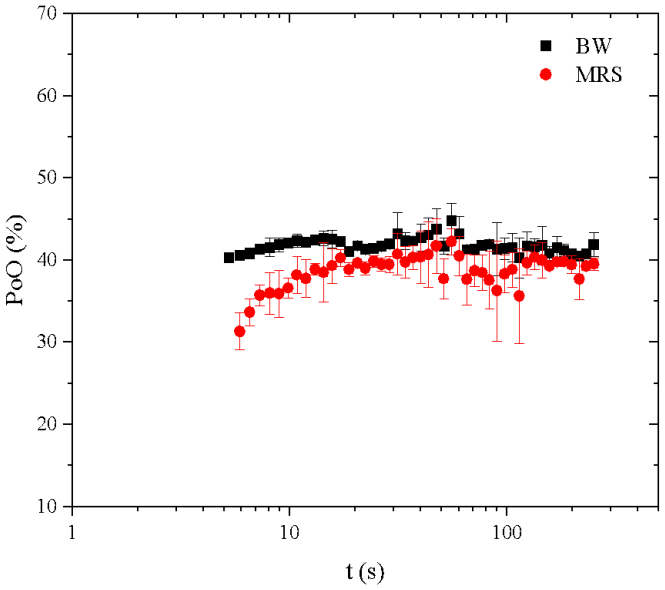

Figure S2.- Time evolution of the mean period (d) computed using the Fast Fourier Transform (FFT) and the autocorrelation (CORR) of a binary mean radial section (like Figure 6c). Particle concentration $\phi = 10$ vol%. External magnetic field strength $H = 10.81$ kA·m^{-1}. Rim shear rate $\dot{\gamma}_R = 300$ s^{-1}.

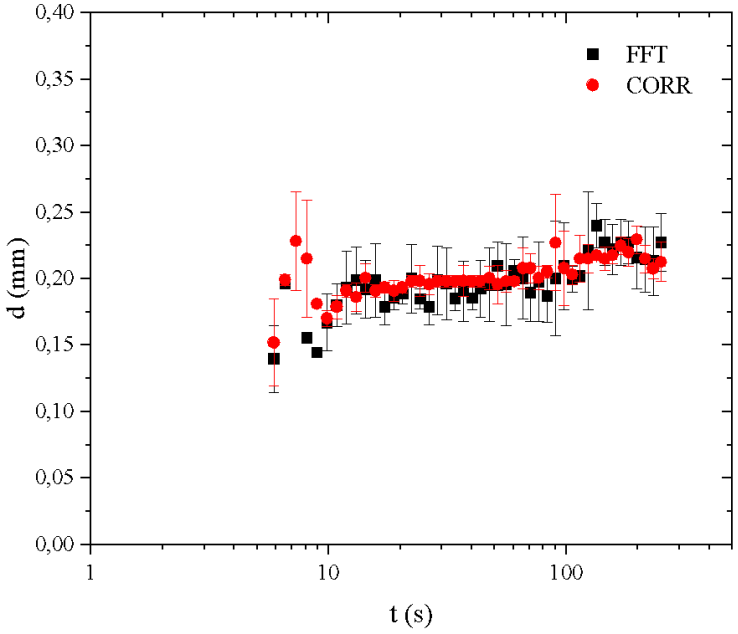

Figure S3.- Shear stress versus time response for a MR fluid ($\dot{\gamma}_R = 500\ s^{-1}$) and a silicone oil ($\dot{\gamma}_R = 430\ s^{-1}$). Both measurements (in triplicates) show a large scattering at the beginning of the experiment indicating that it is mostly generated by the short acquisition times. However, the fact that the scattering is slightly larger in the case of the MR fluid suggests that the particles are also playing a role.

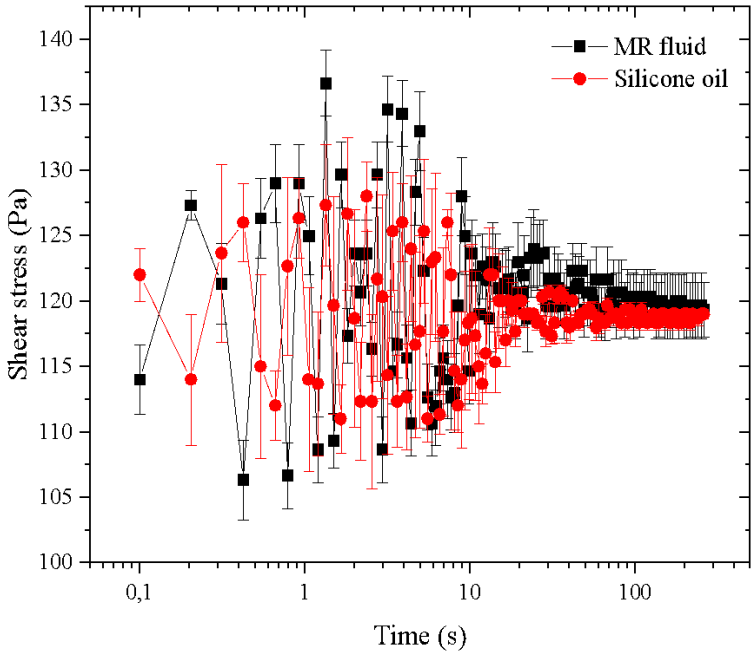

Figure S4.- (a) Shear stress versus time curves in start-up tests under different rim shear rates. Top: lin-log representation. Bottom: lin-lin representation. (b) Summary images for start-up experiments under different rim shear rates ranging from 100 to 500 s^{-1}. Particle concentration $\phi = 10$ vol%. External magnetic field strength $H = 10.81$ $kA \cdot m^{-1}$. The X axis corresponds to the time as measured from the beginning of the start-up experiment. The Y axis corresponds to the distance from the center of the geometry in the radial direction. Stable layers are only observed for $\dot{\gamma}_R \geq 300$ s^{-1}. Results for $\dot{\gamma}_R = 300$ s^{-1} (i.e. at the critical shear rate) demonstrate that at approximately $t = 100$ s the stress momentarily departs from its steady value showing a noticeably drop. Such a drop is associated to the onset of an instability that destroys the layers for radii larger than 3 mm. This clearly demonstrates that the layers play a crucial role supporting the shearing stress under flow. Instabilities do not appear at the same time for different repetitions.

a1)

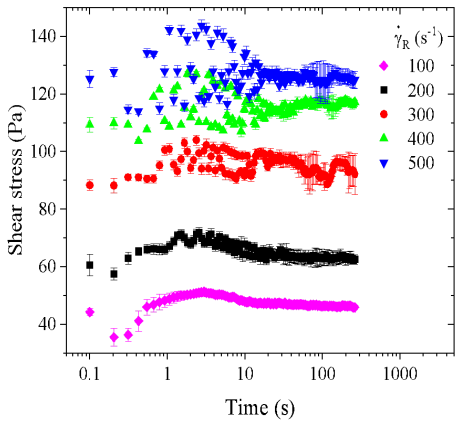
Shear stress (Pa)
Time (s)
$\dot{\gamma}_R$ (s^{-1})
100
200
300
400
500

a2)

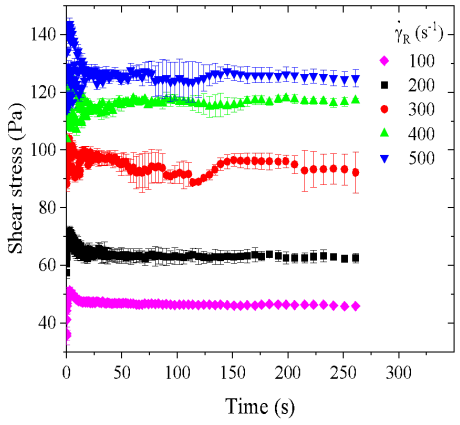
Shear stress (Pa)
Time (s)
$\dot{\gamma}_R$ (s^{-1})
100
200
300
400
500

b)

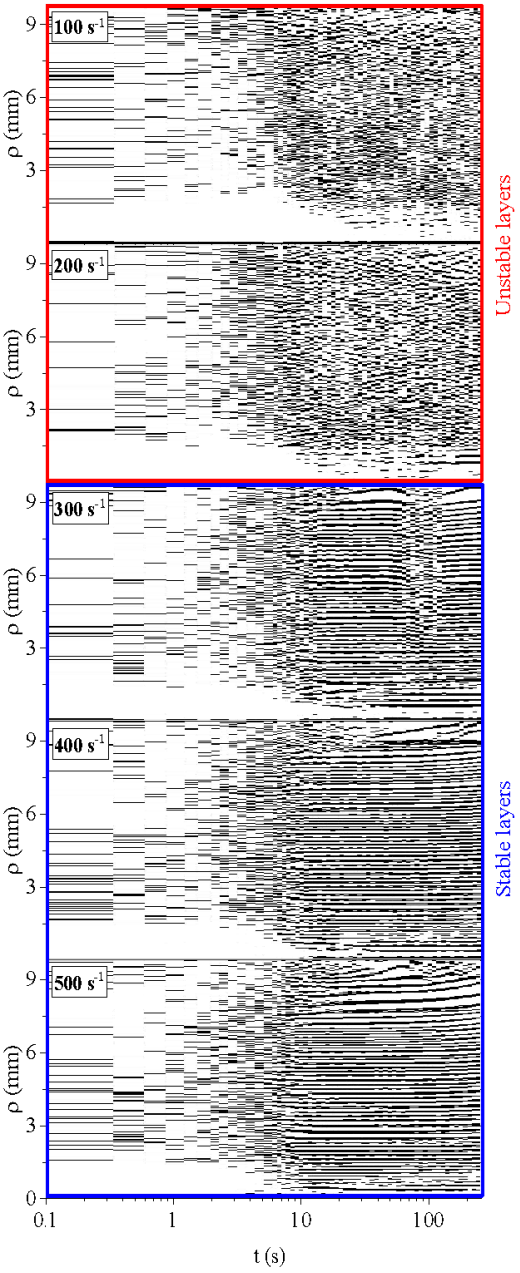
100 s^{-1}
200 s^{-1}
300 s^{-1}
400 s^{-1}
500 s^{-1}
ρ (mm)
t (s)
Unstable layers
Stable layers

Figure S5.- Rim shear stress versus time and summary pictures for rim shear rates of $\dot{\gamma}_R = 100,\ 200\ and\ 400\ s^{-1}$. The layered pattern does not stabilize even after a long time when the shear rate is lower than the critical one (i.e. for 100 and 200 s^{-1}). Particle concentration $\phi = 10$ vol%. External magnetic field strength $H = 10.81\ kA{\cdot}m^{-1}$.